Origin of Surface-Driven Passive Liquid Flows

*Sumith YD and Shalabh C. Maroo**

Department of Mechanical and Aerospace Engineering, Syracuse University, Syracuse, NY 13244, USA.

Corresponding Author

*Email: scmaroo@syr.edu

ABSTRACT

Passive liquid flow occurs in nature in the transport of water up tall trees, and is desired for high-heat flux removal in thermal management devices. Typically, liquid-vapor surface tension is used to generate passive flows (e.g., capillary and Marangoni flows). In this work, we perform a fundamental molecular study on passive liquid flow driven by the solid-liquid surface tension force. Such surface tension values are first estimated by placing a liquid film over the surface and simulating various surface temperatures, followed by which, passive flow simulations are performed by differential heating of the liquid film over the surface. Very strong passive liquid flows are obtained which enable steady-state, continuous and high-heat flux removal close to the maximum theoretical limit as predicted by the kinetic theory of evaporation. Non-dimensional empirical relations are developed for surface tension gradient, flow velocity, and evaporation rate.

TOC GRAPHICS

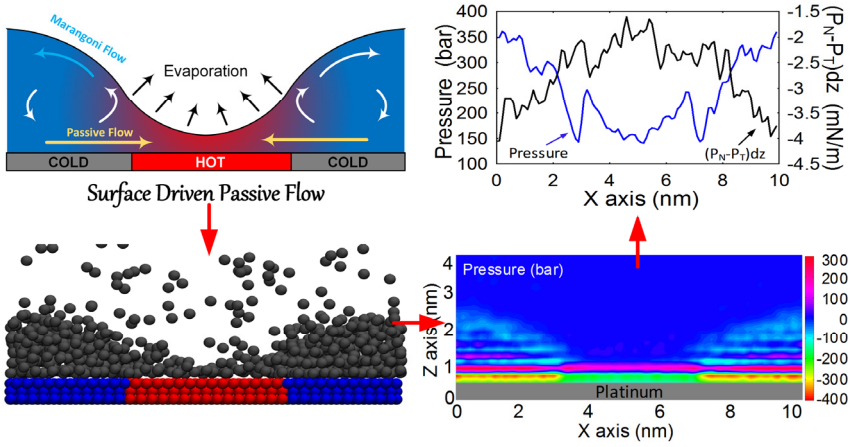

KEYWORDS:

Molecular Dynamics, Passive Flow, Surface Heating, Surface Tension, Evaporation

INTRODUCTION

Transport of liquid is an essential phenomenon occurring in many natural and man-made systems. Nature utilizes passive flow of liquid towards this purpose, for e.g., water flows up a height of over 100 m in redwood trees[1] which requires a pressure difference of ten atmospheres. Macro-scale man-made systems typically use externally driven mechanisms, such as pumps, to drive the liquid. However, with the advent of nanotechnology, liquid transport in small scale systems is not trivial due to the large pressure drops occurring at such length scales, thus making externally driven flows impractical. An important application is the thermal management of electronics and energy conversion devices (e.g. concentrated photovoltaics), where high-flux cooling is desired by continuous supply of liquid to the hot surface followed by its evaporation. Inspired from nature, passive liquid flow is the only possible practical solution, albeit at higher and well-controlled flow rates to avoid system failure.

Passive liquid flows, driven by liquid-vapor surface tension forces, have been extensively studied in the past. Primary examples include liquid-vapor surface tension driven Marangoni flows [2-5] and capillary flows [6-9]. A handful of experimental designs have been tested for heat flux removal based on passive flow generated by capillary pressure[10-12]. The previous studies have shown heat fluxes of 46 W/cm^2 [13], 96 W/cm^2 [10], and a maximum of 1200 W/cm^2 [14]. However, the maximum theoretical limit of heat flux is ~20,000 W/cm^2 from the kinetic theory of evaporation [15], and moving towards a larger fraction of this goal would require stronger passive flows.

This work focuses on surface-driven passive liquid flow, which occurs in all phase change phenomena at the microlayer (Fig. 1), but has not yet been investigated in literature. The phenomenon occurs at the nanoscale, and when coupled with its fluidic and dynamic nature,

makes it nearly impossible to study with current non-intrusive experimental techniques. Hence, under such a scenario, molecular dynamics (MD) simulations are the ideal method to investigate this phenomenon. However, surface-driven flows require the modeling of temperature differential on the same surface, which was lacking in MD. The authors developed such surface-heating algorithms for argon[16] and water[17] thus making this fundamental study possible. These algorithms were also validated to capture the correct mechanism to transfer the heat from a solid surface to liquid droplets and films. In this work, we first characterize the solid-liquid interface at different surface equilibrium temperatures, followed by differential heating of a liquid film to create a meniscus and attain passive surface-driven flow due to solid-liquid surface tension gradient.

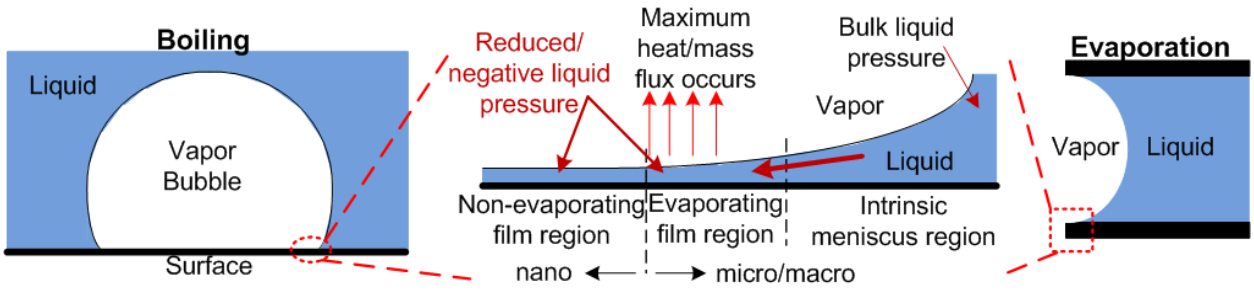

Figure 1: Microlayer occurs in all phase-change processes and consists of three multi-scale regions. Passive flow occurs due to the pressure difference generated between the nano non-evaporating film region and the macro bulk meniscus region.

SOLID LIQUID SURFACE TENSION ESTIMATION

Very few data exist for solid-liquid surface tension, which is the driving force of surface-driven passive flows. In order to understand the near surface dynamics, we need to characterize the system by estimating pressure, surface tension, density and velocity. Thus, as the first step,

equilibrium MD simulations were performed to determine the solid-liquid surface tension at the argon-platinum interface. These studies will serve as the baseline case study of surface tension, pressure, density and velocity in the absence of surface thermal gradient to which we can compare the passive flow simulations and understand the variation of these thermodynamic properties. A 6 nm argon film was placed on a 4 x 4 nm platinum surface, and seven different cases were studied with surface temperatures varying from 90 K to 150 K in steps of 10 K (Fig. 2a). The well-established Lennard-Jones interaction parameters for argon-argon and argon platinum were taken from literature [16]. Our surface heating algorithm [16] is used to simulate the heat transfer between platinum and argon. Simulations were performed for 1000 ps using our in-house molecular dynamics (MD) code written in C++, in which the last 500 ps was used for data sampling and ensemble averaging of various quantities like pressure tensor components, temperature, and density. We used our recently developed 2D pressure calculation algorithm [18] to estimate these quantities. For all the cases and results in this work, we used a spread radius of 0.2 nm with a bin size of 0.1 nm. Surface tension is calculated from the 2D grid values of pressure tensor components and averaged over time. The one dimensional (Z-axis) quantities are obtained from the 2D grid data (XZ plane) by averaging it along X-axis. The system does not have property variations along the homogeneous Y-axis direction. The density of argon is averaged along lateral (X-axis) direction and its variation along vertical direction (Z-axis) is shown in Fig. 2b. Inset of Fig. 2b shows the near-surface density fluctuations. Similarly, the ensemble averaged local surface tension is also calculated along vertical direction and shown in Fig. 2c for different surface temperatures. These plots show that the high dense layers appears near the surface due to the attractive force of the dense atoms of the surface (~20 times denser

than liquid), and dictate the surface tension. Thus, the solid-liquid surface tension manifests itself in a system based on the strength of the solid-liquid molecular attraction.

We estimated the solid-liquid surface tension by integrating the quantity shown in Fig. 2c from 0.5 nm to 1.5 nm, and from 4 nm to 10 nm to obtain the solid-liquid and liquid-vapor surface tensions, respectively. The estimated surface tension values and their variation with temperature are shown in Fig. 2d for Argon-Argon (AA) and Argon-Platinum (AP) for different estimation schemes used: 2D Hardy's method [18] (HD) and Irving Kirkwood's 1D (IK) method [19], and for different cutoff radii: 1.1 nm and 1.8 nm. The results of AA surface tension is compared with experimental NIST data (AA-NIST) [20], and shows good agreement. Results from the well established IK based analysis is also calculated for comparison with our 2D Hardy method, and shows no variation if we chose appropriate parameters like spread radius and bin size. These results for AA liquid-vapor surface tension validate our in-house code and our 2D pressure estimation method. Further, to the best of our knowledge, this is the first time in literature that solid-liquid surface tension is estimated directly from MD simulations.

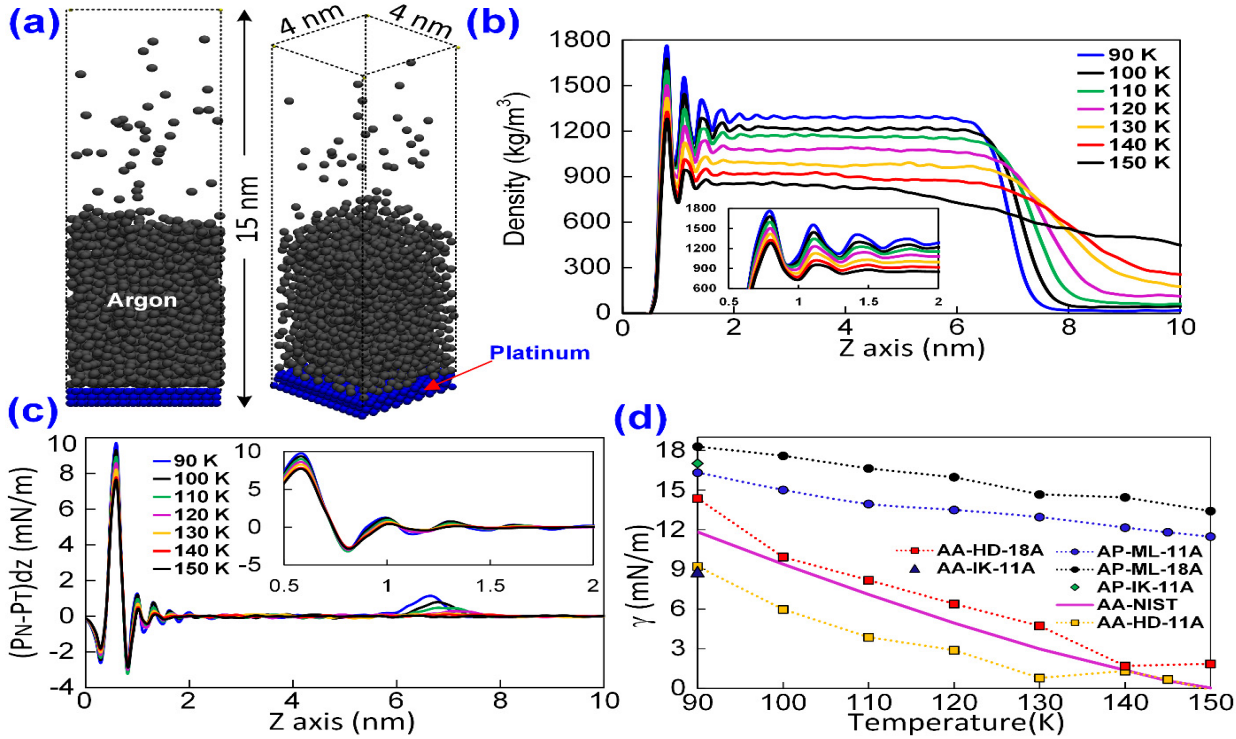

Figure 2. Molecular simulation of liquid argon film heated at different surface temperatures. (a) Equilibrated simulation domain of liquid film of 4×4×6 nm on platinum plate at 90 K. (b) Density of the fluid domain along vertical (Z) axis for different surface temperatures. The inset shows the zoomed view of density fluctuations near the surface. (c) Difference of normal and tangential pressure multiplied by bin size at different surface temperatures along the Z axis. The inset shows the zoomed view near surface. The integral of these curves results in the surface tension. (d) Surface tension of argon-argon (AA) and argon-platinum (AP) using Hardy (HD) [18] and Irving-Kirkwood (IK) methods [19] for the equilibrated cases. The surface tension of argon-platinum for the monolayer (ML) next to the surface is shown for different cutoff radii.

PASSIVE FLOW SIMULATIONS

Next, we perform non-equilibrium MD simulation to attain surface-driven passive flows. Differential surface heating is required in this case, and the 2D pressure algorithm (validated in

Fig. 2d) is essential to estimate the lateral solid-liquid surface tension and relate it to the strength of the passive flow. The simulation domain consists of a 1.5 nm thin argon film on top of a 10 x 4 nm platinum surface (Figs. 3a-b). A 4 nm region at the center of the platinum surface is heated (red color) while the remaining surface is always kept at 90 K (blue color) in all simulations. Seven simulation cases are run for different temperatures of the heated region: 100 K to 150 K in steps of 10 K, and also for 145 K. In the last 500 ps of these simulations, the thermodynamic quantities are averaged and estimated. A snapshot of the MD domain is shown in Fig. 3c for the heated region temperature of 145 K. As the heated region partially evaporates the liquid present at the center, a meniscus forms similar to the microlayer (Fig. 1). Time averaged 2D density, absolute pressure and temperature of the system is shown in Figs. 3d-f respectively. A crystalline-like dense layering of argon liquid can be seen next to the surface in the cooler region (Fig. 3d) due to the strong attractive force of surface atoms. The thin monolayer of argon in the central heated region is also seen in Fig. 3d but with a lower density compared to the cooler region. This difference in density affects the pressure contours (Fig. 3e) where liquid pressure in the monolayer is lower in the heated region compared to the cooler region. Figure 3f shows the temperature distribution in the heated and cooler liquid regions, as well as the overall domain.

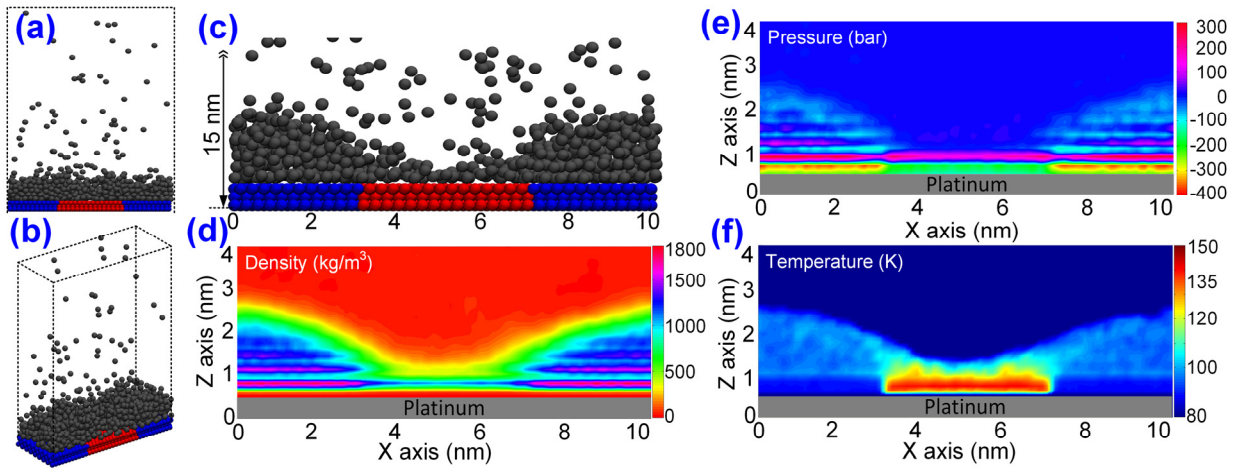

Figure 3. Differential heating of argon film on platinum surface. (a, b) Simulation domain with thin (1.5 nm) argon film initially at 90 K on a 10 × 4 nm platinum surface. The red region is heated, while the blue region is kept at 90 K. (c) Equilibrated liquid film when the heated region is at 145 K; the film does not completely evaporate. (d-f) Two-dimensional density, pressure and temperature contours averaged over 500 ps of simulation.

In order to assess the existence of passive liquid flow, the velocity of the fluid from the MD simulation is mapped into an Eulerian field using 2D interpolation [18]. The simulation domain is divided into three imaginary zones A, B and C as shown in the Fig. 4a. The size of the arrows represents the magnitude of the velocity, and the velocities in zone B are scaled by 3 times to enhance the visibility of the flow field. We observe the formation of a strong passive flow from the cold regions to the heated region in the monolayer next to the surface (Figs. 4a-c). The heated surface causes evaporation of argon and creates a surface tension variation on the surface. This surface tension gradient force drives and dictates the magnitude of the passive flow (further analyzed later). We also see the Marangoni flow along the liquid-vapor interface causing liquid to flow from the heated to cooler regions. However, as seen in Figs. 4b-c, the liquid-solid surface-tension driven passive flow is much stronger than the liquid-vapor surface-tension driven Marangoni flow.

RESULTS AND DISCUSSION

As the liquid-solid surface-tension gradient is the main driving force for the passive flow, we directly estimate this gradient along the surface. The surface tension gradient is determined by taking the difference of surface tension between the heated and cold regions. Surface tension in

monolayer along X axis is obtained by summing $(P_N - P_T)dz$ from 0.5 nm to 1.5 nm along Z axis and shown in Fig. 5a when hot surface was at 145 K (P_N is the normal pressure, P_T is the tangential pressure and dz is the slab thickness). This average surface tension variation is then averaged for a 2 nm span in heated region and a 4 nm span in cold regions along X-axis, and their difference is estimated to get the average surface tension gradient. A second graph in the Fig. 5a shows the variation of absolute pressure in monolayer along X-axis. Figure 5b shows the comparison of argon-platinum surface tension estimated at the monolayer and over a 1 nm film thickness from these non-equilibrium simulations of film evaporation with those obtained from equilibrium simulations of Fig. 2. The passive flow in the system is occurring as the tangential pressure component is much higher along the monolayer in the heated region than the cool region, thus leading to a surface tension gradient along the surface and the occurrence of passive flow. The tangential pressure is also found to be greater than the normal pressure in the monolayer. Further, the surface tension estimated is different when considering only the monolayer compared to when considering a thicker film (of 1 nm) above the surface (Fig. 5b), due to the reduction of surface effect as we move away from the monolayer in this weak van der Waals force driven system. Please refer to supporting information for plots on pressure components. Thus, surface-driven passive flow is expected to occur in the region where the surface tension values are negative, and can occur in thicker films for liquid such as water due to presence of strong Coulomb force.

Overall, the temperature gradient along with evaporation creates a surface tension gradient resulting in pressure gradient which augments the flow of rewetting the surface. The reduced pressure in the hot region, existence of high negative surface tension in monolayer hot region compared to cold region, and continuous re-wetting of the hot surface due to the strong pressure

difference present near to the surface support the existence of a strong passive flow, and enable a continuous and steady heat removal process in the system.

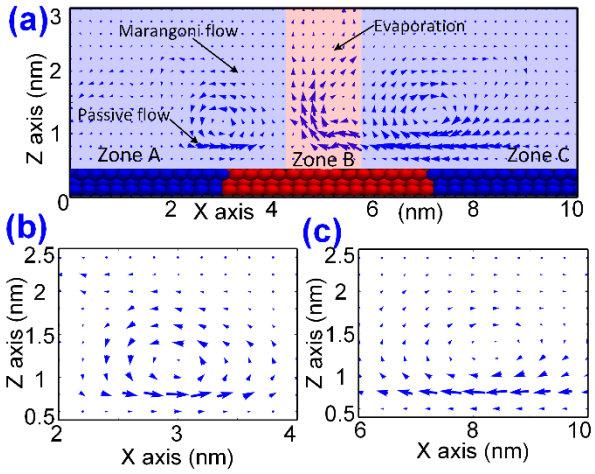

Figure 4. (a) Two-dimensional time-averaged velocity mapping of the domain showing passive liquid flow driven by the solid-liquid surface tension gradient. Size of the arrows indicates the magnitude of the velocity. Velocities of Zone B are scaled by 3 times to that of Zones A and C for better clarity. (b, c) Close-up view of the circulation and passive flow regions at either sides.

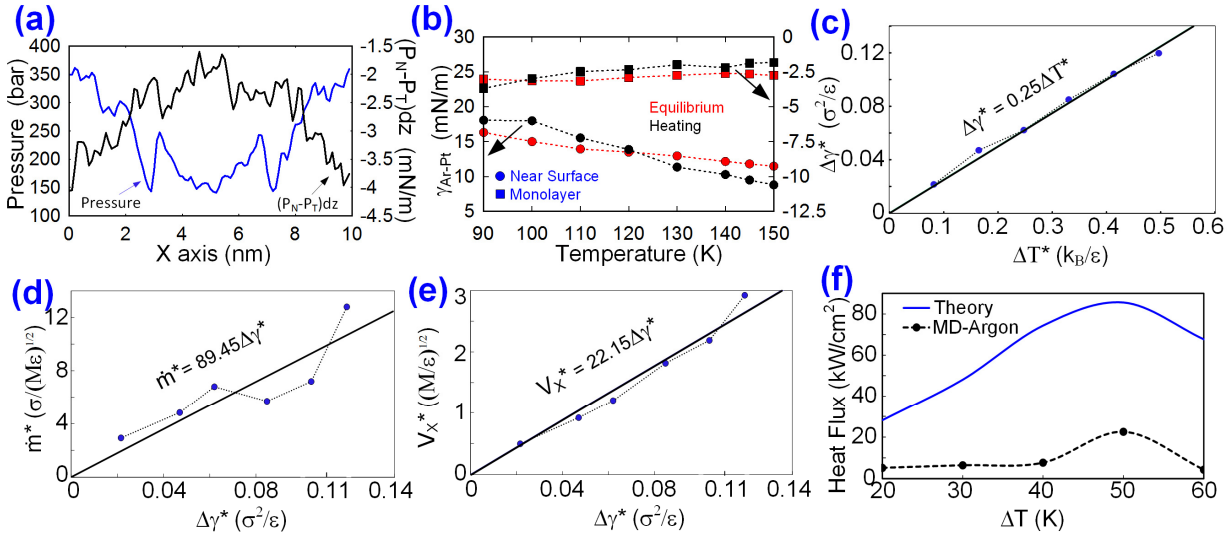

Figure 5. Analysis of solid-liquid surface tension driven passive liquid flows. (a) Surface tension (black line) and average pressure (blue line) of argon-platinum along X axis for monolayer region; the gradient present in this region, along with the effect of evaporation causes passive

liquid flow (color online). (b) Comparison of near surface and monolayer surface tension of argon-platinum (AP) estimated for both equilibrium and passive flow cases. The upper two curves with square markers show the monolayer surface tension, while the bottom two refers to surface tension averaged from 0.5 nm to 1.5 nm. The red curves (color online) represent equilibrium baseline study and black curves (color online) show passive flow (heating) cases. (c) Non-dimensional surface tension gradient versus surface temperature gradient. (d) Non-dimensional passive flow average velocity along X axis and its dependency on surface tension gradient. (e) Non-dimensional mass flow rate of passive flow with surface tension gradient. (f) Continuous steady state heat flux removed from the surface due to liquid evaporation. The plot shows the comparison between maximum possible heat flux from kinetic theory[15] to that estimated from our simulations.

We also relate the surface tension gradient with temperature gradient (Fig. 5c), and find the relation to be linear, as expected from continuum equations. We further analyze the steady-state flow velocity, mass evaporation rate, and the heat flux and relate it to the solid-liquid surface-tension gradient and surface temperature difference. Quantities are non-dimensionalized so that the results can be extended for other non-polar solid-liquid combinations. Figure 5d shows the average passive liquid flow velocity, determined using the analysis from Fig. 4, as a function of the surface tension gradient, which shows very high flow velocities can be achieved. We estimate the average evaporation rate (from Zone B of Fig. 4) by performing a control volume analysis (please refer to the supplementary document) and relate it to the surface-tension gradients for different surface temperatures. The evaporation rate is determined based on the density and velocity averaged on the top boundary of control volumes (the control volumes for

different heating temperatures are shown in supplementary material.). Such empirical relations can be used to design the operating conditions of passive-flow driven thermal management devices as it can help predict the surface tension gradient and mass flow rate generated for a desired surface temperature gradient.

Based on the attained evaporation rate and the heating area, we estimate the stead-state averaged evaporative heat flux obtained in the system. As mentioned earlier, the heated surface area is 4×4 nm where the surface-heating algorithm is applied. The resulting values are compared (Fig. 5f) against the theoretically possible maximum heat flux [15] values obtained from the equation: $q_{max} = \rho_g h_{fg} \sqrt{RT/2\pi}$ .The heat flux, in kW/cm^2, is shown as a function of temperature difference between heated and cold regions. The simulation results follow the theoretical trend where the heat flux peaks at the temperature difference of 50 K. Beyond that, the temperature of heated region reaches critical temperature of argon thus resulting in a decline. The peak heat flux obtained in simulations is 22.5 kW/cm^2 and is orders of magnitude higher than the maximum reported values in experiments. To the best of our knowledge, this is the first study where steady-state, continuous and passive high-heat flux removal close to the theoretical limit is obtained.

The values of the passive evaporative heat flux is expected to be much higher in the case of water due to the polar nature of the liquid and presence of hydrogen bonding result in high negative pressures near to the surface, which is part of ongoing and future work. Further, we are extending the surface heating algorithm [17] to LAMMPS[21] to study passive flow of water on silicon dioxide surfaces.

CONCLUSION

In conclusion, we used molecular dynamics simulations to understand the origin of surface driven passive flows which are generated due to solid-liquid surface tension gradients. We quantified the solid-liquid surface tension for various surface heating temperatures, and developed empirical relations for surface tension gradient, flow velocity, and evaporation rate. We attained continuous heat flux removal close to the theoretical limit of evaporation completely driven by passive liquid flow. Thus, strong passive flows can be generated by choosing appropriate surface and liquid combinations to create desired solid-liquid surface tension gradients, along with evaporation based reduction in pressure and density with increase in surface temperature. Experimental estimation of surface tension for various solid-liquid combinations needs to be pursued towards designing passive and ultra-high heat flux thermal management devices.

SUPPORTING INFORMATION

The supporting information is available free of charge on the ACS publication website at DOI:

Pressure characterization, two dimensional velocity plots, density plots and control volume analysis details are discussed in detail in this document.

AUTHOR INFORMATION

Corresponding Author

*Email: scmaroo@syr.edu

FUNDING: This material is based upon work supported by the National Science Foundation under Grant No. 1454450.

Notes: The authors declare no competing financial interest.

REFERENCES

1. Tyree, M. T. Plant hydraulics: the ascent of water. *Nature* **2003,** *423*, 923-923.

2. Kundan, A.; Plawsky, J. L.; Wayner Jr, P. C.; Chao, D. F.; Sicker, R. J.; Motil, B. J.; Lorik, T.; Chestney, L.; Eustace, J.; Zoldak, J. Thermocapillary Phenomena and Performance Limitations of a Wickless Heat Pipe in Microgravity. *Phys. Rev. Lett.* **2015,** *114*, 146105.

3. Tam, D.; von ARNIM, V.; McKinley, G.; Hosoi, A. Marangoni convection in droplets on superhydrophobic surfaces. *J. Fluid Mech.* **2009,** *624*, 101-123.

4. Zhang, K.; Ma, L.; Xu, X.; Luo, J.; Guo, D. Temperature distribution along the surface of evaporating droplets. *Phys. Rev. E* **2014,** *89*, 032404.

5. Cai, Y.; Zhang Newby, B.-m. Marangoni flow-induced self-assembly of hexagonal and stripelike nanoparticle patterns. *J. Am. Chem. Soc.* **2008,** *130*, 6076-6077.

6. Pratt, D. M.; Kihm, K. D. Binary fluid mixture and thermocapillary effects on the wetting characteristics of a heated curved meniscus. *J. Heat Transfer* **2003,** *125*, 867-874.

7. Huang, D.; Ma, L.; Xu, X. The capillary outward flow inside pinned drying droplets. *Int. J. Heat Mass Transfer* **2015,** *83*, 307-310.

8. Nie, C.; Frijns, A. J.; Mandamparambil, R.; den Toonder, J. M. A microfluidic device based on an evaporation-driven micropump. *Biomed. Microdevices* **2015,** *17*, 1-12.

9. Wang, Y.; Ma, L.; Xu, X.; Luo, J. Combined effects of underlying substrate and evaporative cooling on the evaporation of sessile liquid droplets. *Soft matter* **2015,** *11*, 5632-5640.

10. Xiao, R.; Maroo, S. C.; Wang, E. N. Negative pressures in nanoporous membranes for thin film evaporation. *Appl. Phys. Lett.* **2013,** *102*, 123103.

11. Wheeler, T. D.; Stroock, A. D. The transpiration of water at negative pressures in a synthetic tree. *Nature* **2008,** *455*, 208-212.

12. Ranjan, R.; Patel, A.; Garimella, S. V.; Murthy, J. Y. Wicking and thermal characteristics of micropillared structures for use in passive heat spreaders. *Int. J. Heat Mass Transfer* **2012,** *55*, 586-596.

13. Adera, S.; Antao, D.; Raj, R.; Wang, E. N. Design of micropillar wicks for thin-film evaporation. *Int. J. Heat Mass Transfer* **2016,** *101*, 280-294.

14. Palko, J.; Zhang, C.; Wilbur, J.; Dusseault, T.; Asheghi, M.; Goodson, K.; Santiago, J. Approaching the limits of two-phase boiling heat transfer: High heat flux and low superheat. *Appl. Phys. Lett.* **2015,** *107*, 253903.

15. Gambill, W. R.; Lienhard, J. H. An Upper Bound for the Critical Boiling Heat Flux. *J. Heat Transfer-Trans. ASME* **1989,** *111*, 815-818.

16. Maroo, S. C.; Chung, J. N. A novel fluid-wall heat transfer model for molecular dynamics simulations. *J. Nanopart. Res.* **2010,** *12*, 1913-1924.

17. YD, S.; Maroo, S. C. Surface-Heating Algorithm for Water at Nanoscale. *J. Phys. Chem. Lett.* **2015,** *6*, 3765-3769.

18. YD, S.; Maroo, S. C. Two-Dimensional Pressure Formulation in Molecular Dynamics. *submitted* **2016**.

19. Irving, J. H.; Kirkwood, J. G. The Statistical Mechanical Theory of Transport Processes .4. The Equations of Hydrodynamics. *J. Chem. Phys.* **1950,** *18*, 817-829.

20. Lemmon, E.; McLinden, M.; Friend, D. Thermophysical Properties of Fluid Systems. *NIST chemistry webbook, NIST standard reference database* **2005,** *69*.

21. Plimpton, S.; Crozier, P.; Thompson, A. LAMMPS-large-scale atomic/molecular massively parallel simulator. *Sandia National Laboratories* **2007,** *18*.